QUANTIFYING REACTIVE FLOW-INDUCED PORE EVOLUTIONS IN MICROPOROUS CARBONATE CORES USING X-RAY MICRO-COMPUTED TOMOGRAPHY

Jafar Qajar[1], Nicolas Francois[2] & Christoph H. Arns[1]
[1] School of Petroleum Engineering, University of New South Wales, Sydney, Australia
[2] Dept. of Applied Mathematics, Australian National University, Canberra, Australia

This paper was prepared for presentation at the International Symposium of the Society of Core Analysts held in Aberdeen, Scotland, UK, 27-30 August, 2012.

ABSTRACT

The acid stimulation of carbonate reservoirs results in substantial changes of the pore structure, especially when the reactive flow is accompanied by the release and migration of fine particles. In addition to the amount of mineral dissolved, the spatial distributions of dissolution and displaced particle zones are important to gain a better understanding of the evolution of rock properties and for the effective design and implementation of acidizing processes. However, the inherent complexity of most carbonates due to the presence of micro- and nanopores has limited the characterization of the evolution of carbonate microstructure at the pore scale.

This paper proposes an integrated technique based on the registration of pre- and post-dissolution micro-computed tomography (μ-CT) images, three-phase segmentation and 2D intensity histograms of these images to examine the trend of grey-scale changes of image voxels along the flow direction. We carry out reactive flow experiments on two limestone samples of varying complexity. The set of all possible voxel density evolution scenarios is introduced and the distribution of each evolution region is used to spatially analyse the dissolution process along the length of the cores. The results show that the μ-CT technique can quantitatively characterise the dissolution process and the associated migration of fines despite the presence of sub-resolution features in the images and provides insight into pore scale reactive displacement mechanisms and their effects on the evolution of rock properties.

INTRODUCTION

Recent progress in the development of X-ray μ-CT makes it possible to directly visualize and quantify the dissolution-induced evolution of the pore structure of complex carbonate rocks at the micrometre scale [1-5]. However, many challenges behind the implementation of this approach still exist, which limit the usability of μ-CT data. The voxel-scale interpretation of successive images of a sample, in particular if they are taken at different conditions, requires an ability to spatially register images at voxel scale accuracy. In addition, details of small pores below the voxel size of images have not been considered in previous studies. This is especially important for most carbonate sediments since microporosity is an important porosity type in them.

A 3D registration technique has recently been developed, which allows voxel perfect overlays of tomographic images of successively altered core samples [6]. This allows the voxel per voxel comparison of X-ray densities and associated quantities between registered images. In this paper we undertake reactive flow experiments of carbonate samples covering different dissolution patterns and define voxel evolution scenarios at the pore scale using greyscale density data provided from images in pre- and post-dissolution states. 2D intensity histograms of segmented registered images are used to quantify these voxel evolution scenarios. We also measure the permeability changes and explain the effect of longitudinal variations of the dissolution and particle displacement regions on the permeability change.

MATERIALS AND EXPERIMENTAL METHODS

Samples

The reactive flow experiments were conducted on two carbonate cores with different rock types, whose measured properties are listed in Table 1. The first sample (Rock 1) is a Savonniere limestone, an oolitic carbonate with moderate permeability and a wide range of pore sizes. The second sample (Rock 2) is a Shuaiba limestone which is much less permeable and exhibits a bimodal pore size distribution. Figure 1 shows examples of 2D μ-CT slices and MICP curves of the core samples. About 50% of the porosity of Rock 1 and the major porosity of Rock 2 (~80%) are only accessible via sub-resolution pores. A significant contribution to porosity in Rock 2 comes from intercrystalline micropores, i.e. pores in the range of 100 nm to 4 μm, but pores bigger than 100 μm are also present.

Experimental Methods

Reactive flooding of cores was undertaken using 0.25 M ethylenediaminetetraacetic acid (EDTA) at pH 12 and ambient conditions. The structure of EDTA is typically represented by H_4Y where Y indicates the ligand. Under high pH (>12) conditions, the reaction responsible for calcite dissolution is given by [7]:

$$Y^{-4} + CaCO_3 \rightleftharpoons CaY^{-2} + CO_3^{-2} \quad (1)$$

The core samples were first dried and imaged using the μ-CT facility [8] and sealed on the sides using a Fluoropolymer heat shrink and vacuum saturated with deionized water afterwards. EDTA was injected by a motor-controlled syringe pump, initially at a higher rate for a few seconds for quick replacement of water with EDTA inside the sample before injecting at the desired rate. The pressure drop along the core length was monitored by a differential pressure transducer. Permeability was calculated using injection rate and pressure drop as a function of injection time using Darcy's law. The injection of EDTA was terminated after significant changes in permeability (more than two times increase) occurred in the core (Table 1). Finally, the core was detached from tubing, dried in an oven and imaged again. Figure 2 illustrates the measured permeability responses of the cores in terms of the ratio of the instant permeability to the initial permeability as a function of the injection time. When the injection begins at the desired values, the permeability of both samples decreases first and then steadily increases as

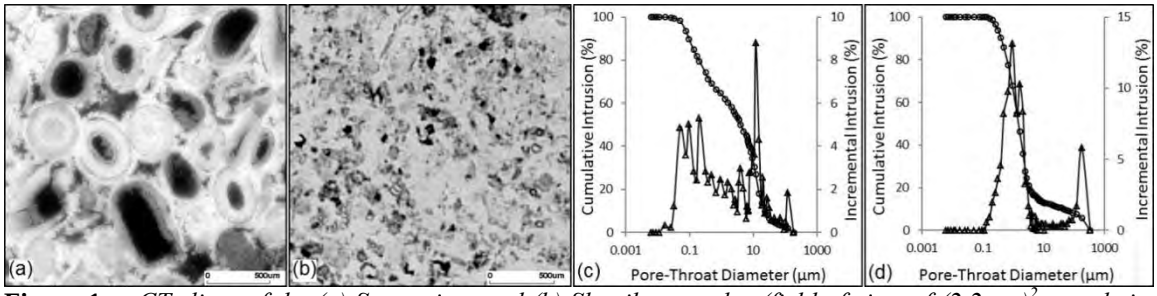

Figure 1. *µ-CT slices of the (a) Savonniere and (b) Shuaiba samples (field of view of (2.2mm)^2, voxel size ~4.4µm) and MICP curves of sister plugs of the (c) Savonniere and (d) Shuaiba samples.*

injection time increases. This behaviour is unlike the steady increasing permeability responses previously obtained for coreflood experiments with EDTA [7]. The early decrease in permeability suggests particle displacement and effective pore clogging during the early stage of the experiments for both samples.

Analysis of µ-CT Data and Microporosity Assignment

Images of each sample, prior and after the experiments, were taken near the centre of the cores (close to the inlet) with ~ (9 mm)^3 FOV. Tomograms in each state were composed of 2048^3 voxels. An image registration technique was used to superpose the tomogram of the altered sample to the tomogram of the original unaltered sample in 3D [6]. The resulting registered tomograms of the samples correspond to datasets with the size of ~ (7.3 mm)^3 at voxel sizes of 4.49 and 4.33 µm for Rock 1 and Rock 2, respectively. Even though image registration allows us to compare common features in images at different states, several artefacts make voxel-by-voxel comparisons of registered images difficult [9]. Here we minimize geometrical errors by using the same acquisition geometry and associated resolution. We assume that for this case the X-ray source spot size stayed constant between acquisitions leading to comparable influences of material in one voxel on surrounding voxels. The X-ray intensity was found to be slightly different in the two acquisitions. In order to operate on the same grey scales, we locate recognizable unaltered voxels in both images and assume that both images have regions of pore or

Table 1. *Measured properties of the samples before and after the reactive flow experiments.*

	Rock 1	Rock 2
Diameter (mm)	7.0	7.0
Length (mm)	20.6	16.9
Initial porosity (%)	30.6	21.0
Final porosity (%)	42.6	~22.5
Initial water permeability (md)	58.6	3.2
Final water permeability (md)	154.8	7.3

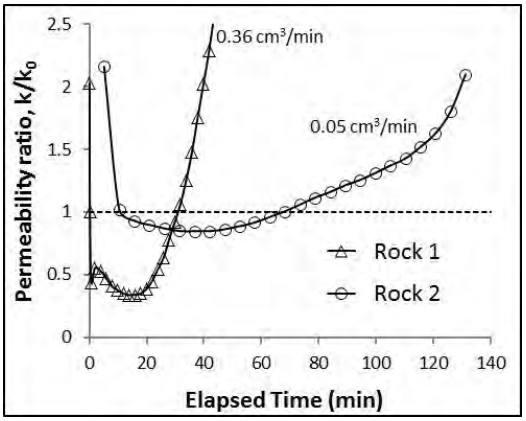

Figure 2. *Permeability responses from reactive flow experiments with high-pH EDTA.*

grain with unchanged density in the course of dissolution, which defines the outer bounds of the resultant X-ray density histogram. The registered tomograms were then rescaled to a common greyscale with intensities 0 to 255 by adjusting the minimum and maximum intensity values of both images at fixed values using a linear interpolation procedure. We used a nonlinear anisotropic diffusion filter to reduce noise to comparable levels and enhance the quality of images [10]. Figure 3 shows the intensity histograms of images after rescaling and filtering. The post-dissolution intensity histograms of both samples show clear bimodal distributions, whereas the pre-dissolution histograms spread out to the low X-ray attenuation due to the larger amount of sub-resolution porosity. To accurately describe the porosity of the sample, it is necessary to assign sub-resolution porosity from image data. In this paper, a three-phase segmentation method was used to partition images into resolvable macropore, intermediate and grain phases [11, 12]. The intermediate phase was therefore divided into 102 separate phases based on their relative attenuation. A microporosity value (between 0 and 1) was assigned to each voxel in the intermediate phase based on a linear interpolation of the attenuation between the maximal value of the identified macropore phase and minimum value of the grain phase [13].

Method for Quantifying Evolution of Individual Voxels

The presence of a great number of intermediate voxels in both images makes direct comparison of pre- and post-dissolution 1D histograms difficult. In this paper, we propose to use 2D intensity histograms of registered images to quantitatively investigate the evolution of each image voxel and provide a reflection of the actual regional mass changes. In this respect, the 2D histogram is constructed by plotting the value of segmented image intensity from pre-dissolution image against the corresponding value from the registered post-dissolution image, voxel by voxel. The resulting 2D histogram represents the probability that a voxel evolves from a particular pre-intensity to a particular post-intensity range. Since the segmented pre- and post-dissolution images contain four types of voxel –grain, macropore, relatively higher intensity intermediate, and relatively lower intensity intermediate– 16 possible voxel evolutions are expected. We classify all changes of voxel values into 12 voxel evolution scenarios in which the void fraction (or solid fraction) of a voxel increases, decreases or remains unchanged

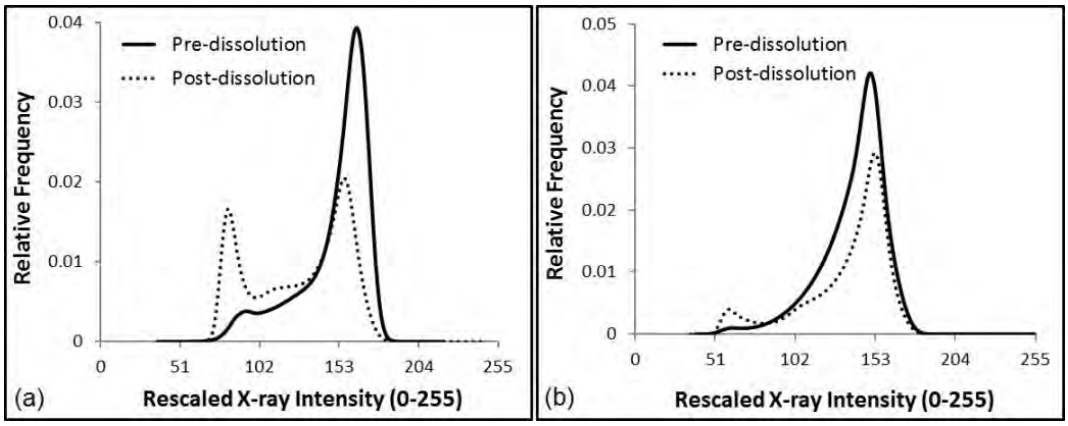

Figure 3. *Rescaled intensity histograms of registered filtered images for (a) Rock 1and (b) Rock 2.*

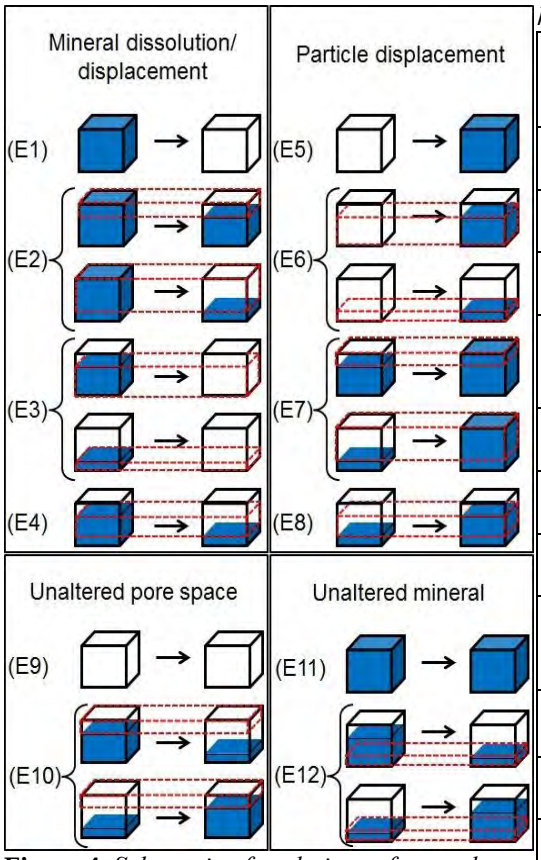

Figure 4. *Schematic of evolutions of a voxel giving rise to various evolution patterns.*

Table 2. *Voxel evolution scenarios based on the 2D histogram of the registered images.*

Voxel evolution scenario	Physical/chemical phenomena occurred during the experiment	Evol-ution label
Grain to macropore	Complete grain dissolution/displacement	E1
Grain to intermediate	Partial grain dissolution/displacement	E2
Intermediate to macropore	Complete solid dissolution/displacement	E3
Higher intensity to lower intensity intermediate	Partial solid dissolution/displacement	E4
Macropore to grain	Complete macropore filling	E5
Macropore to intermediate	Partial macropore filling	E6
Intermediate to grain	Complete micropore filling	E7
Lower intensity to higher intensity intermediate	Partial micropore filling	E8
Macropore to macropore	Unaltered macropore	E9
Micropore to micropore	Unaltered micropore	E10
Grain to grain	Unaltered grain	E11
Solid to solid	Unaltered solid	E12

(Figure 4 & Table 2). In Table 2, grain refers to a voxel which only contains mineral and solid represents the part of a voxel of intermediate density filled partially with mineral. Similarly, macropore refers to a voxel which is completely void space and microporosity denotes the void part of an intermediate voxel. The proposed evolution scenarios can be reduced to 4 general evolution regions as indicated in Figure 4: *mineral dissolution/displacement region* which refers to voxels (or part of voxels) that are initially solid but will finally be dissolved or displaced; *particle displacement region* which shows voxels (or part of voxels) that are in the pore space but will finally be occupied by mobilized particles; *unaltered pore space* and *mineral regions* which represent voxels (or part of voxels) that belong to pore space or solid mineral from the beginning to the end.

RESULTS AND DISCUSSION

3D Geometry of the Dissolution Patterns

Examples of registered slices along the length of the samples in pre- and post-dissolution states are shown in Figure 5. Visual observations reveal two different dissolution regimes within the core samples. Images for Rock 1 show that the reactive fluid was consumed over large parts of the mineral surface area leading to a large increase of porosity. Intra-

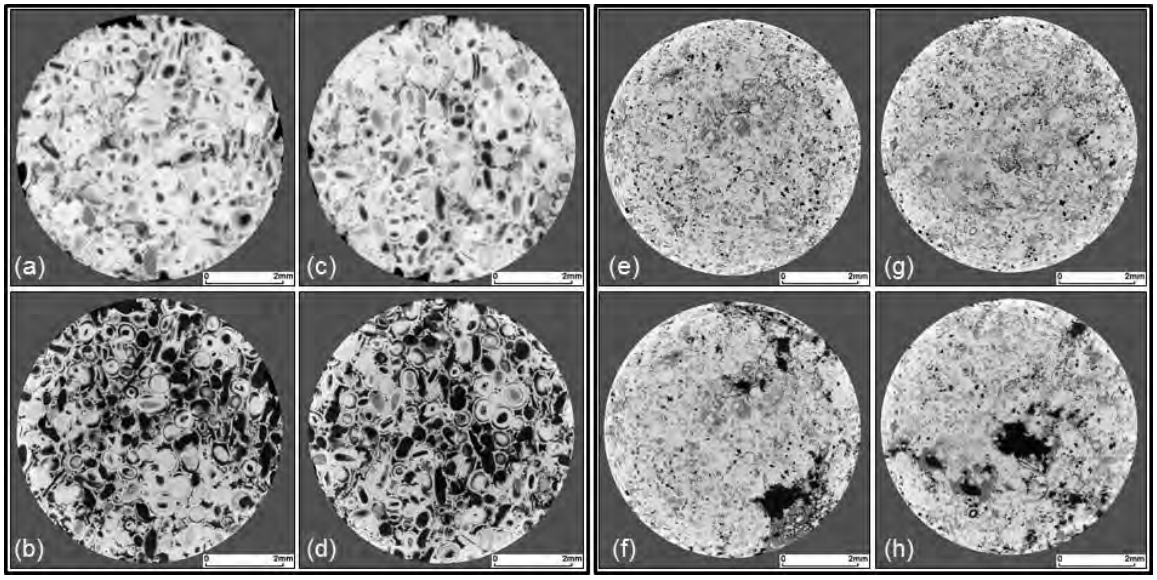

Figure 5. *Slices of registered images of Rock 1 (a-d) and Rock 2 (e-h) before (top) and after (bottom) the experiments at different distances to the injection face: (a-b) 8.64,(c-d) 11.13, (e-f) 6.91 and (g-h) 9.41 mm.*

and inter-moldic pore-filling and less dense cement was preferentially dissolved. Oomoldic and interooidal pores were enlarged and the connectivity of pores considerably increased. Observations of the whole post-dissolution tomogram revealed that the dissolution-induced pores were largely distributed within the core with no visible major flow paths resulting in a quasi-uniform dissolution regime. In contrary, the reactive fluid was consumed over small parts of the mineral surface area of Rock 2 leading to the formation of a few conical wormholes and a small increase of porosity. The wormholes were initiated at the injection face and propagated through the core. The precision of the registered images also allowed us to observe particle mobilization after the reactive flow experiments. Figure 6 illustrates examples of close-up images from the 3D tomograms. It can be observed that some pore space was filled with particles after the experiments.

Table 3 illustrates the values of the macro, micro, and total porosity of the samples prior and after the dissolution experiments obtained from three-phase segmentation of the images. The lab measured initial porosity of both samples and final porosity of Rock 1

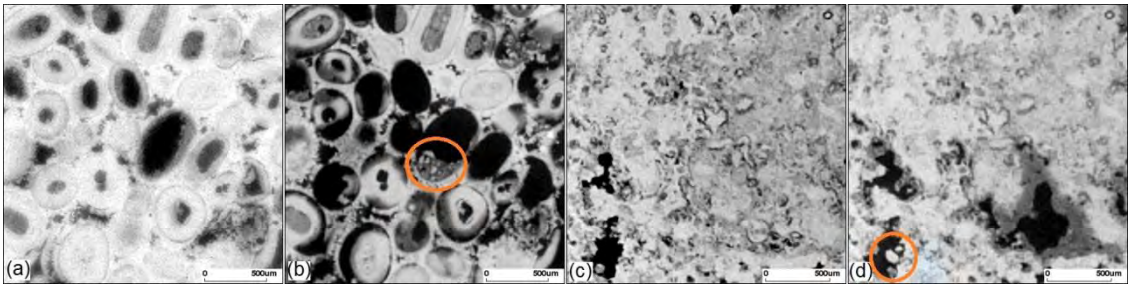

Figure 6. *Close-up slices of 3D images of (a) Rock 1and (c) Rock 2 prior to the experiments. (b) and (d) the corresponding registered slices after the experiments for Rock 1 and Rock 2, respectively. Evidences of particle mobilization are shown with orange circles.*

Table 3. *Values of different types of image-based porosity before and after the dissolution experiments.*

		φ_{macro} (%)	φ_{micro} (%)	φ_{total} (%)
Rock 1	Pre-dissolution	12.5	15.3	27.8
	Post-dissolution	23.5	17.6	41.1
Rock 2	Pre-dissolution	2.2	20.1	22.3
	Post-dissolution	7.6	18.4	26.0

are in good agreement with the corresponding image-based total porosity despite experimental measurement errors and partial imaging of the samples. However, the lab measured final porosity of Rock 2 is significantly lower than the total porosity calculated from the post-dissolution image of Rock 2. Observations of Rock 2 after the dissolution showed that the wormholes did not break through the core, i.e. no dissolution spots were observed on the outlet face of the sample. Helical μ-CT scanning of the entire post-dissolution Rock 2 also confirmed that the wormholes only penetrated to 15.7 mm from the inlet. We imaged the part of the sample close to the reactant injection face (at about 2 mm from the inlet face of the sample) which contains larger wormholes while the lab measured porosity represents an average value of the porosity over the whole sample. In addition, the porosity of the post-dissolution Rock 2 could not accurately be measured by water saturation method because the reactive flow partly damaged the injection face of the core and fine particles were displaced during vacuum saturation.

Characterization of Voxel Evolution Scenarios

To evaluate the trend of greyscale changes of voxels, the segmented datasets are divided into several sub-volumes along the flow axis, each with 100 voxels in thickness, and the 2D histograms are computed for each sub-volume using MATLAB. Figure 7 shows the computed 2D histograms for the selected sub-volumes with choosing 10 intensity intervals (bins) along each of the intensity axes (a total of $10^2 = 100$ bins). Each bin in the 2D intensity histogram represents the previously described voxel evolution scenarios in Table 2 and Figure 4. Observations of the 2D histograms in Figure 7 show that aside from unaltered regions, the most frequent voxel evolutions are differently distributed in samples. For the reactive flow experiment in Rock 2, the most frequent voxel evolution is in the vicinity of the upper left part of the main diagonal of the histograms, i.e. lower intensity intermediate to higher intensity intermediate. Conversely, frequent evolution scenarios in Rock 1 reside in three sides of the histograms, i.e. grain/intermediate to macropore, grain to intermediate and intermediate to grain. This indicates that the evolution of flow pathways and particle movement occurred through different mechanisms during the experiments resulting in more dissolution than particle displacement in Rock 1, and vice versa for Rock 2.

The volume fraction of each voxel evolution scenario based on the total possible number of bins (i.e., 104 bins since each voxel can take an integer value between 0 and 103) was calculated and is shown in Table 4. The mineral dissolution/displacement region includes voxels belonging to the particle displacement region. The change in porosity (mass) measured in the laboratory reflects the net mineral dissolution (mineral dissolution minus particle displacement). If we define the net mineral dissolution ratio (NDR) as the mass

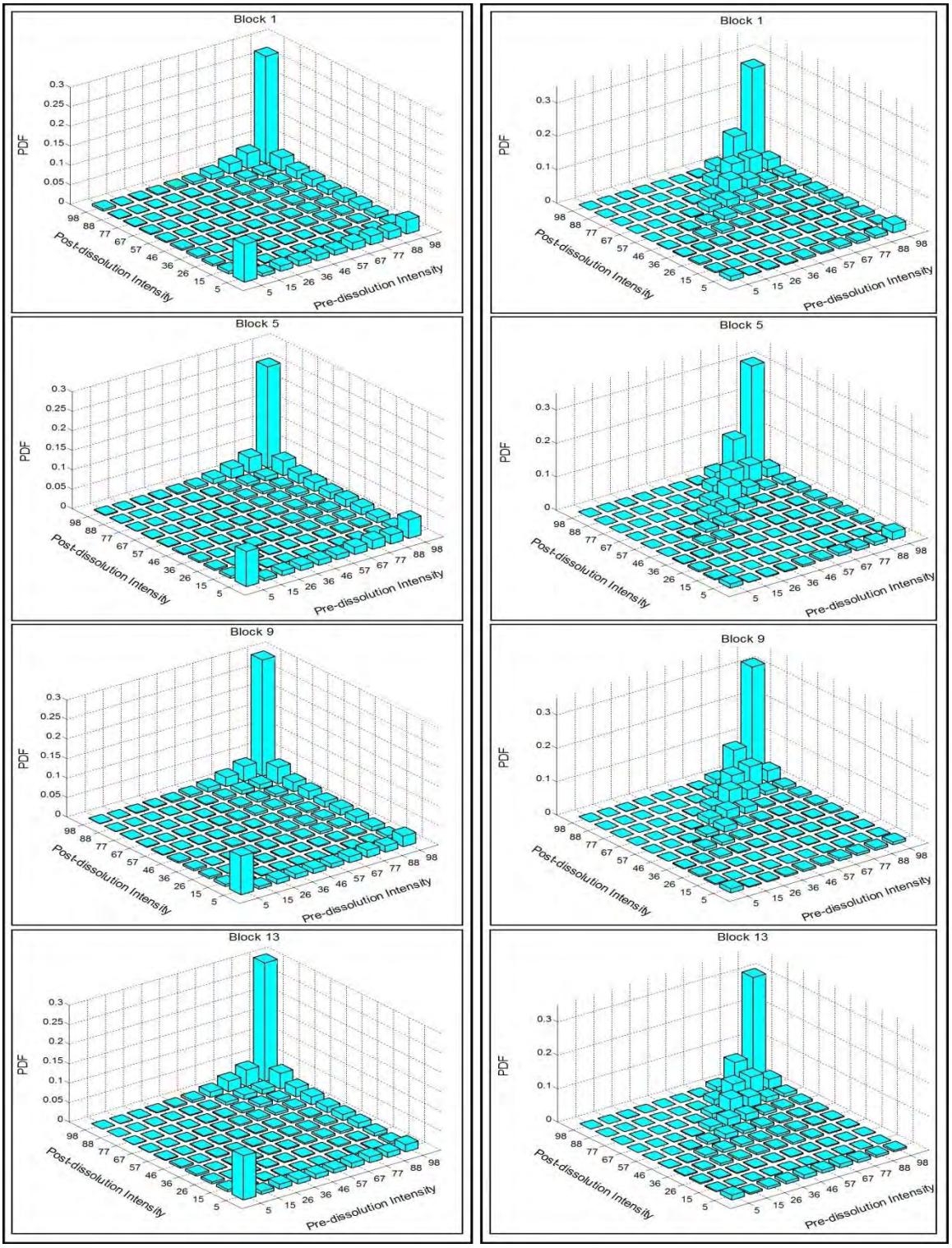

Figure 7. *2D probability distribution functions of pre-dissolution intensity vs. post-dissolution intensity for selected blocks of (left) Rock 1 and (right) Rock 2 along the flow axis. Block 1 is closest to the inlet for each sample and the centres of adjacent blocks are spaced 0.449 and 0.433 mm apart for Rock 1 and Rock 2, respectively.*

Table 4. *Average volume fraction of voxel evolution scenarios for the performed experiments.*

Evol-ution label	Ave. Fraction (%)		Total evolution (Fraction %)
	Rock 1	Rock 2	
E1	1.98	0.68	Mineral dissolution/ displacement (Rock1=18.22) (Rock 2=8.29)
E2	4.47	1.20	
E3	6.87	3.52	
E4	4.90	2.89	
E5	0.13	0.00	Particle displacement (Rock 1=5.00) (Rock 2=5.24)
E6	0.98	0.26	
E7	2.07	0.48	
E8	1.81	4.49	
E9	9.61	1.11	Unaltered pore space (Rock 1=22.66) (Rock 2=17.08)
E10	13.05	15.97	
E11	22.77	15.90	Unaltered mineral (Rock 1=54.12) (Rock 2=69.39)
E12	31.35	53.49	

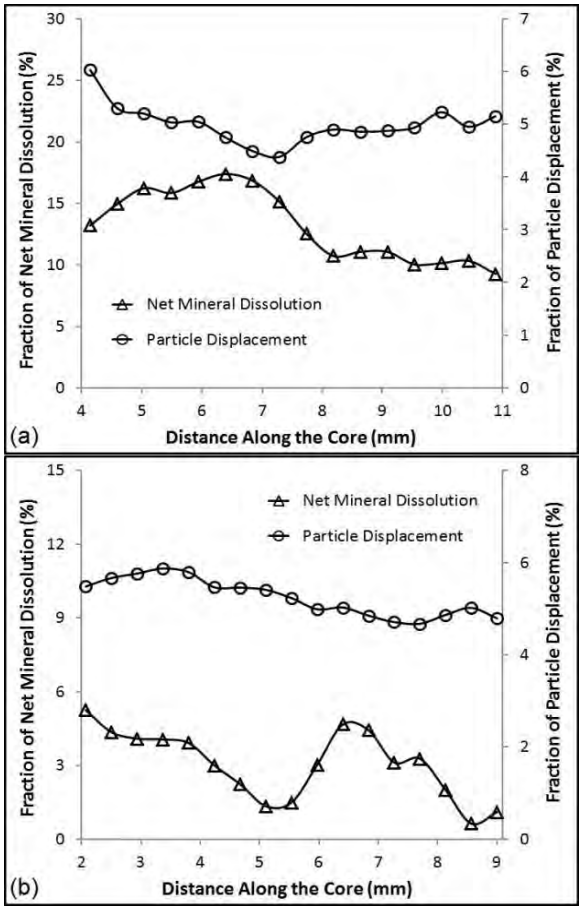

Figure 8. *Variation of the fraction of net mineral dissolution and particle displacement along the flow axis for (a) Rock 1 and (b) Rock 2.*

difference divided by the initial mass of the core, the following equation holds assuming monomineralic rock:

$$\mathrm{NDR} = \frac{\Delta m}{m_0} \quad \frac{\sum_{i=1}^{4} E_i - \sum_{i=5}^{8} E_i}{\sum_{i=1}^{4} E_i \quad \sum_{i=11}^{12} E_i}. \tag{1}$$

where E_i is the fraction of the evolution region *i* defined in Table 2. Since the reactive flow altered the structure of Rock 1 quasi-uniformly, we can validate the calculated NDR with the experimental value despite the fact that the entire length of the sample could not be imaged at the time of the initial experiment. According to the lab measured initial and final porosity of Rock 1 (Table 1), the calculated NDR (18.3%) is in good agreement with the experimental value (17.3%). As expected for Rock 2, a large discrepancy between the calculated and the experimental values of NDR was observed due essentially to the fact that we imaged part of the sample that contains larger wormholes. Using this method, different evolution regions not accessible from lab effluent measurements can be quantified from μ-CT images. This is especially important for particle displacement

because dissolution-released particles are a common operational problem during stimulation of carbonate reservoirs which causes well plugging. The 2D histograms of registered images allow us to effectively incorporate microporosity in the calculation of local porosity changes at the voxel scale. The proposed method can be generally applied to any alteration process. In this way, each voxel evolution scenario essentially represents a region with porosity increase, porosity decrease, or unchanged porosity.

Figure 8 shows the variation of the fractions of voxel evolution regions along the flow axis. For both rocks, dissolution of minerals is maximized at some distance with respect to the inlet side. Comparison of the net mineral dissolution curves shows that more dissolution occurred in the vicinity of the inlet of Rock 1 compared to Rock 2. Conversely, particle displacement curves indicate that deposition of particles mainly occurred in pores far from the inlet boundary of Rock 1 and vice versa for Rock 2. Temporal evolution of permeability (Figure 2) shows that permeability decreased at first for both samples before it steadily increased during the experiments. At early times of the EDTA injection, the dissolution occurred more at the inlet of the core samples. At this stage, fine particles were released and displaced along the flow paths as near-inlet grains were dissolved and clogged some of the pore throats which resulted in early permeability decline. This was more pronounced for Rock 1, as indicated in Figure 2, since the reactant penetrated to the larger parts of the sample and hence more fine particles were released and clogged pore throats. As the injection time increased, mobilized fines were dissolved and displaced. As a result, pore throats were declogged accompanying dissolution of grains and increasing pore opening, which as a whole led to a steady increase in permeability at later times. For Rock 1, the released fines that were preserved from complete dissolution were deposited at greater distances. In this case, highly distributed flow paths created by the reactive flow make it possible for fine particles to displace at greater distance along the sample length. At the inlet of Rock 2, we observed the opposite behaviour. Since the reactive flow created a few major flow paths in Rock 2 and concerning Rock 2 as a tight-textured rock with very low permeability, a few particles were able to displace along the flow paths and hence they were mainly deposited near the inlet of the core.

Effect of Microporosity on the Quantification of the Evolution Regions

The results of the proposed method based on the three-phase segmentation and the 2D histogram of registered images are compared with two methods based on simple two-phase segmentation of images. In one method, we segment the registered rescaled images to resolvable macropore and grain phases. In other words, we merge the intermediate phase into the grain phase and ignore microporosity. In the second method, appropriate thresholds for the pre- and post-dissolution images are chosen to conserve total porosity computed by the three-phase segmentation method. These thresholds are first estimated by the arithmetic mean of the peak values from the rescaled histogram and then changed until the measured porosity becomes equal to the total porosity. The results of the fractions of the evolution regions from different methods are shown in Table 5. It is evident from Table 5 that ignoring microporosity causes a significant error in the

Table 5. *Comparison of the fractions of the evolution regions (%) obtained by different methods*

Evolution Region	3-phase segmentation		2-phase segmentation (ignoring microporosity)		2-phase segmentation (conserving total porosity)	
	Rock 1	Rock 2	Rock 1	Rock 2	Rock 1	Rock 2
Mineral dissolution/ displacement	18.2	8.3	13.9	6.6	19.6	10.2
Particle displacement	5.0	5.2	2.9	1.0	5.7	5.8
Unaltered pore space	22.7	17.1	9.6	1.1	21.7	15.8
Unaltered mineral	54.1	69.4	73.6	91.3	53.0	68.3

computation of the fractions of the evolution regions. In this case, the fractions of the dissolution and particle displacement are considerably underestimated. This is because significant part of the original porosity of both samples corresponds to microporosity. Regarding the second two-phase segmentation method, despite improving the results, the fractions of the dissolution and particle displacement are overestimated. Consequently, the method based on the three-phase segmentation and the 2D histograms can give excellent results for quantification of the evolution regions.

CONCLUSIONS

In this paper we applied image registration to establish quantitative techniques for the characterization of reactive flow patterns in carbonates in the presence of microporosity. The main conclusions of this paper are the following:

- We presented results for reactive flow experiments in two carbonate rock types. Two different dissolution regimes, namely wormhole-like and quasi-uniform patterns were observed.
- 2D intensity histograms of the three-phase segmented images were successfully employed to enumerate grey-scale changes from the pre- to post-dissolution images at the voxel scale.
- Several scenarios of dissolution-induced evolutions not accessible from lab effluent measurements were quantified. These scenarios describe dissolution, particle displacement, unaltered pore space and unaltered mineral within a core sample subjected to reactive flow.
- The fraction of the net mineral dissolution determined from image is in good quantitative agreement with the lab measured value.
- Early decrease in permeability was related to pore clogging induced by displacement of dissolution-released particles. The preserved particles from complete dissolution were deposited according to distribution of dissolution-induced pore pathways.

ACKNOWLEDGEMENTS

CHA acknowledges the Australian Research Council for support through an Australian Research Fellowship (DP0881112). The authors acknowledge the member companies of the ANU/UNSW Digital Core Consortium for their support. We thank the National Computing Infrastructure of Australia for computing support through the national merit allocation scheme. We also thank Michael Turner for performing the MICP tests.

REFERENCES

1. Noiriel, C., P. Gouze, and D. Bernard, "Investigation of porosity and permeability effects from microstructure changes during limestone dissolution," *Geophys. Res. Lett.*, (2004) **31**(24).
2. Bernard, D., "3D quantification of pore scale geometrical changes using synchrotron computed microtomography" *Oil Gas Sci. Technol.-Rev. IFP*, 2005. **60**(5): 747-762.
3. Cai, R., W.B. Lindquist, W. Um, and K.W. Jones, "Tomographic analysis of reactive flow induced pore structure changes in column experiments," *Adv. Water Resour.*, (2009) **32**, 1396-1403.
4. Nur, A., T. Vanorio, and E. Diaz, "Effects of Carbon Dioxide Injection in Reactive Carbonates: Computational Rock Physics Basis for Time-Lapse Monitoring," in *Paper SPE 149065, presented at the SPE/DGS Saudi Arabia Section Technical Symposium and Exhibition,* (2011) 15-18 May: Al-Khobar, Saudi Arabia.
5. Gouze, P. and L. Luquot, "X-ray microtomography characterization of porosity, permeability and reactive surface changes during dissolution," *J. Contam. Hydrol.*, (2011) **120-121**, 45-55.
6. Latham, S., T. Varslot, and A.P. Sheppard, "Image Registration: Enhancing and Calibrating X-ray Micro-CT Imaging," in *Paper SCA2008-35, presented at the International Symposium of the Society of Core Analysts*, (2008), 29 Oct-2 Nov: Abu Dhabi UAE.
7. Fredd, C.N. and H.S. Fogler, "Chelating Agents as Effective Matrix Stimulation Fluids for Carbonate Formations," in *Paper SPE 37212, presented at the SPE International Symposium on Oilfield Chemistry*, (1997), 18-21 Feb: Houston, Texas.
8. Sakellariou, A., T.J. Senden, T.J. Sawkins, M.A. Knackstedt, M.L. Turner, A.C. Jones, M. Saadatfar, R.J. Roberts, A. Limaye, C.H. Arns, A.P. Sheppard, and R.M. Sok, "An x-ray tomography facility for quantitative prediction of mechanical and transport properties in geological, biological and synthetic systems," *Developments in X-Ray Tomography IV*, (2004) **5535**, 473-484.
9. Ketcham, R.A., "Computational methods for quantitative analysis of three-dimensional features in geological specimens," *Geosphere*, (2005) **1**(1), 32-41.
10. Sheppard, A.P., R.M. Sok, and H. Averdunk, "Techniques for image enhancement and segmentation of tomographic images of porous materials," *Physica A-Statistical Mechanics and Its Applications*, (2004) **339**, 145-151.
11. Sheppard, A.P., C.H. Arns, A. Sakellariou, T.J. Senden, R.M. Sok, H. Averdunk, M. Saadatfar, A. Limaye, and M.A. Knackstedt, "Quantitative properties of complex porous materials calculated from x-ray μCT images," in *Proc. SPIE, 6318, 631811*, (2006) San Diego, CA, USA.
12. Ghous, A., T.J. Senden, R.M. Sok, A.P. Sheppard, W.V. Pinczewski, and M.A. Knackstedt, "3D Characterisation of Microporosity in Carbonate Cores," *presented at the SPWLA Middle East Regional Symposium*, (2007) 15-19 Apr: Abu Dhabi. UAE.
13. Sok, R.M., T. varslot, A. Ghous, S. Latham, A.P. Sheppard, and M.A. Knackstedt, "Pore Scale Characterization of Carbonates at Multiple Scales: Integration of Micro-CT, BSEM and FIBSEM," in *Paper SCA2009-18, presented at International Symposium of the Society of Core Analysts*, (2009), 27-30 Sep: Noordwijk, NL.